Metallofullerene single-molecule magnet $Dy_2O@C_{2v}$(5)-C_{80} with a strong antiferromagnetic Dy···Dy coupling

Georgios Velkos,‡[a] Wei Yang,‡[a,b] Yang-Rong Yao,[b] Svetlana M. Sudarkova,[a,c] Fupin Liu,[a] Stanislav M. Avdoshenko,*[a] Ning Chen*[b] and Alexey A. Popov*[a]

Supporting Information

Synthesis and isolation of Dy$_2$O@C$_{80}$

Dy$_2$O@C$_{80}$ was synthesized by a modified Krätschmer-Huffman DC arc-discharge method. The carbon rod filled with 1.27 g of Dy$_2$O$_3$ powder and 2.3 g of graphite powder (molar ratio of Dy/C = 1:24) was vaporized under a He/CO2 atmosphere (200 Torr of helium with 20 Torr of CO2 added). The soot was collected and refluxed in carbon disulfide (CS$_2$) under an argon atmosphere for 12 h. The crude extract was treated with TiCl$_4$, which removed most of the empty fullerenes. Dy$_2$O@C$_{80}$ was isolated and purified by multistage high-performance liquid chromatography (HPLC) as in Figure S1.
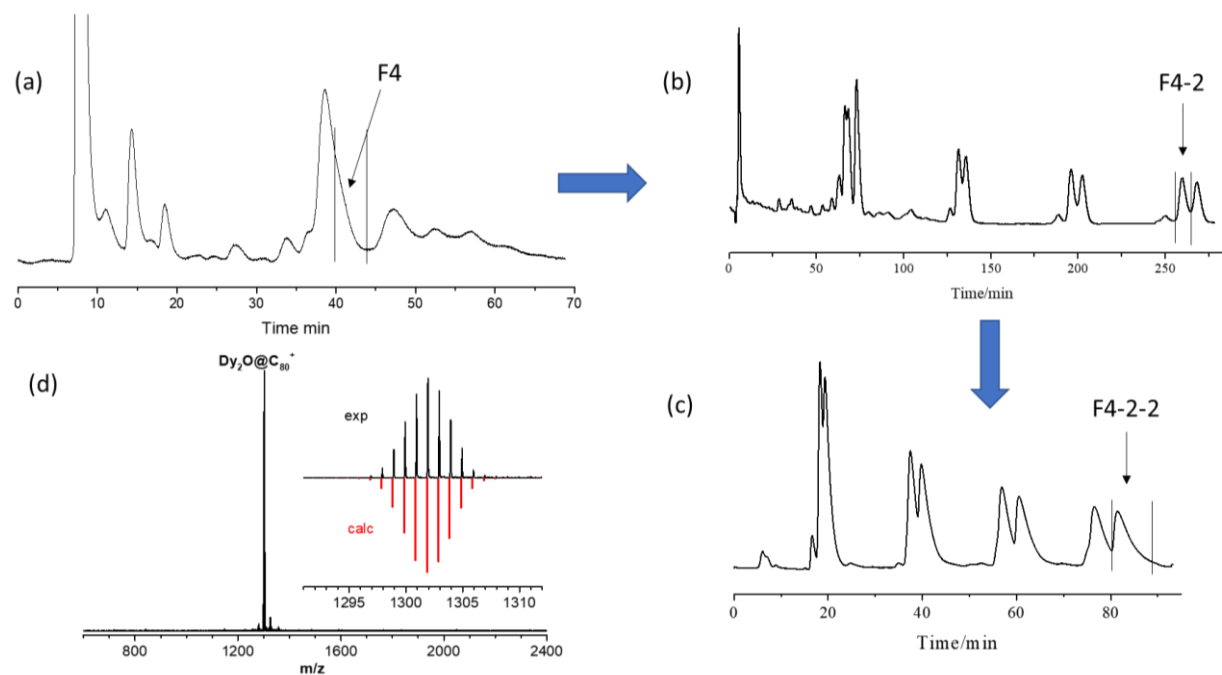
Figure S1. HPLC separation of Dy$_2$O@C$_{80}$. (a) The first stage HPLC chromatogram of the extract on a Buckyprep-M column (Φ = 25 mm × 250 mm, flow rate 10 mL/min). (b) the second stage recycling HPLC chromatogram of fraction F4 on a Buckyprep column (Φ = 10 mm × 250 mm, flow rate 4 mL/min). (c) the third stage recycling HPLC chromatogram of fraction F4-2 on a Buckyprep-D column (Φ = 10 mm × 250 mm, flow rate 4 mL/min). Fraction F4-2-2 is Dy$_2$O@C$_{80}$, Eluent = toluene, detecting wavelength = 310 nm. (d) MALDI-TOF mass-spectrum of Dy$_2$O@C$_{80}$ in a positive-ion mode, the inset shows experimental and calculated isotopic distribution for Dy$_2$O@C$_{80}$.

Crystallographic data

Fullerene molecules usually rotate in the crystals, resulting in a strong disorder. For this reason, the structural elucidation by single-crystal X-ray diffraction is usually performed for co-crystals with the agents, which hinder this rotation. Particular popular co-crystallization agent in fullerene chemistry is Ni^{II} octaethylporphyrin, NiOEP. In this work, $Dy_2O@C_{2v}(5)-C_{80}\cdot Ni(OEP)$ crystals were grown by layering the benzene solution of Ni(OEP) onto the saturated CS_2 solution of $Dy_2O@C_{80}$ in a glass tube. The tube with was then sealed with Teflon and placed into refrigerator with the temperature of 5-10°C. After the two solutions diffused together over a period of 3-4 weeks, the black block crystals were obtained in the tube walls. The crystal was measured at 100 K using synchrotron radiation (0.82653 Å) at the beamline BL17B of the Shanghai Synchrotron Radiation Facility (SSRF). The structure was solved using direct methods and refined on F2 using full-matrix least-squares using the SHELXL2015 crystallographic software package. The disordered solvent molecules are masked with SQUEEZE code. Hydrogens were inserted at calculated positions and constrained with isotropic thermal parameters.

Table S1. Crystallographic information

	$Dy2O@C_{2v}(5)-C_{80}\bullet Ni(OEP)$
Formula	C116 H44 Dy1.97 N4 Ni O
Formula weight	1888.79
Color, habit	Black, block
Crystal system	monoclinic
Space group	P 21/c
a, Å	17.757(4)
b, Å	16.954(3)
c, Å	26.591(5)
α, deg	90
β, deg	107.35(3)
γ, deg	90
Volume, Å	7641(3)
Z	4
T, K	100
Radiation (λ, Å)	0.71073
Unique data (R_{int})	12494
Parameters	1207
Restraints	1438
Observed data	11016
R_1[a]	0.1492
wR_2[b]	0.3428
CCDC No.	2085187

[a]For observed data with $I > 2\sigma(I)$, $R_1 = \frac{\Sigma||F_o|-|F_c||}{\Sigma|F_o|}$. [b]For all data, $wR_2 = \sqrt{\frac{\Sigma\left[w(F_o^2-F_c^2)^2\right]}{\Sigma\left[w(F_o^2)^2\right]}}$.
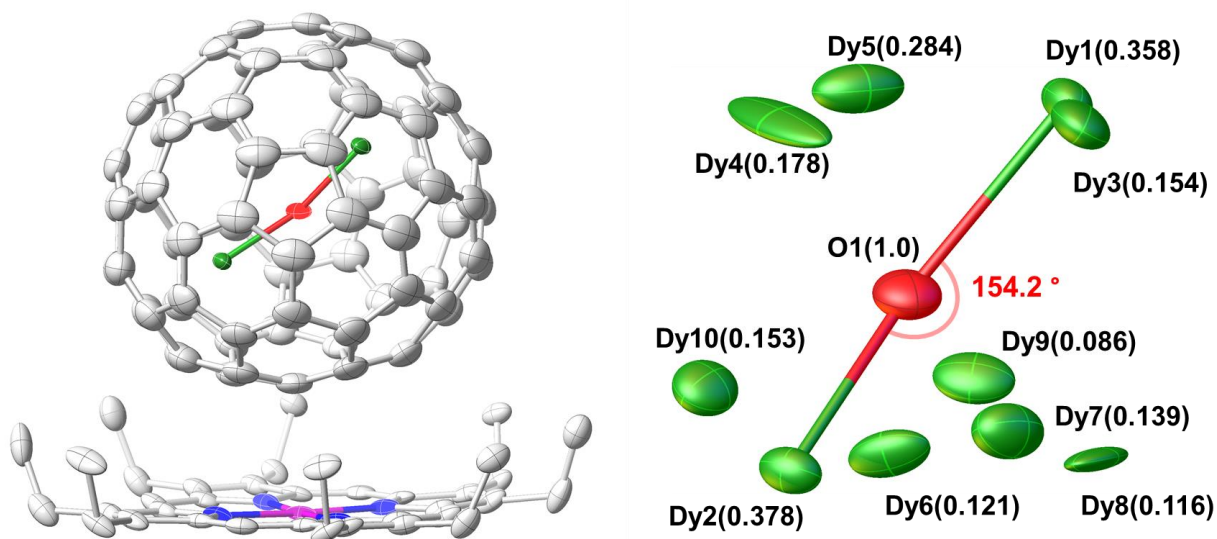
Figure S2. Left: Thermal ellipsoids of $Dy_2O@C_{2v}(5)-C_{80}$ $Ni^{II}(OEP)$ crystals with 30% probability showing only the major dysprosium sites; H atoms and minor Dy sites are omitted, Dy is green, O is red, Ni is purple, N is blue, C is grey. Right: Endohedral Dy_2O unit with disordered Dy sites and selected structural parameters.
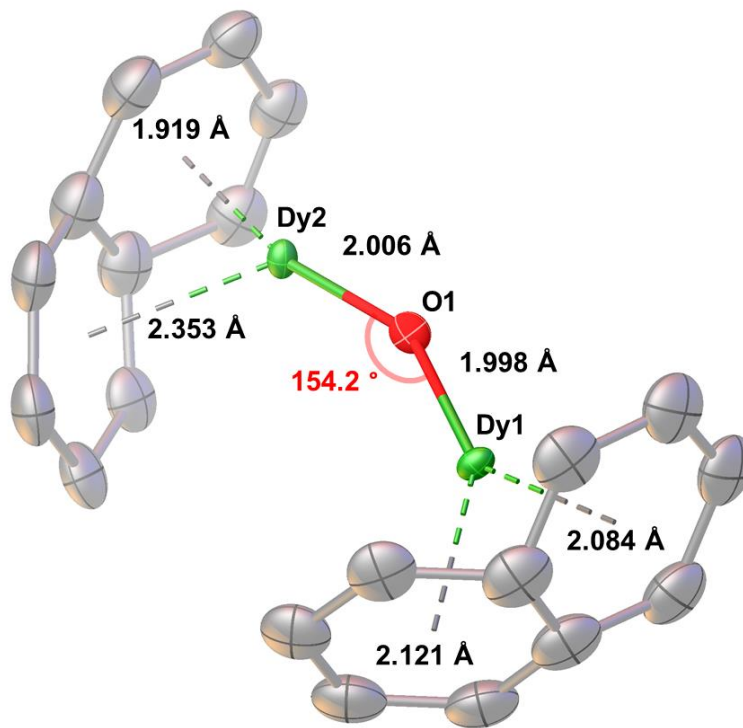
Figure S3. Interaction of the major Dy_2O site with the closest cage moieties.

DFT calculations

(a)

(b)
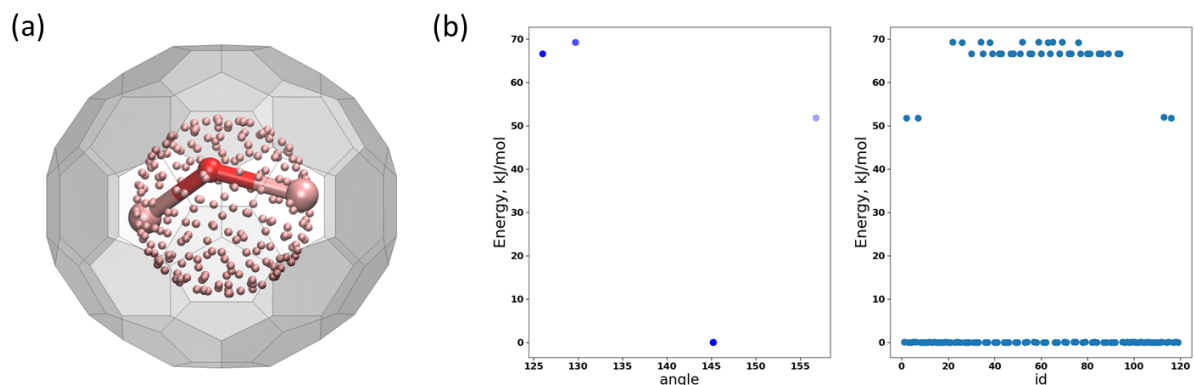
Figure S4. (a) 120 orientations of the Y_2O cluster inside the $C_{2v}(5)$-C_{80} cage (shown overlaid in one figure) used as starting coordinates in the search of stable conformers. DFT optimization of 120 structures gave four unique conformers. (b) Y–O–Y angles and relative energies in four unique conformers and relative energies of all optimized structures

X-ray

conf 1
0.0 kJ/mol

conf 2
49 kJ/mol
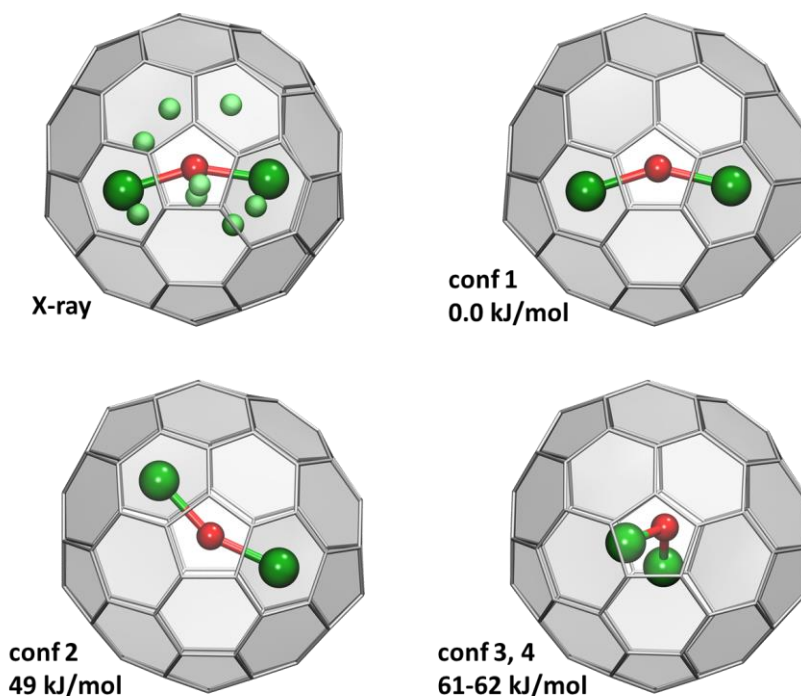
conf 3, 4
61-62 kJ/mol

Figure S5. $Dy_2O@C_{80}$ molecules from the X-ray structure (the site with the largest occupancies of Dy atoms is shown in dark green, whereas minor sites are pale green) and conformers of $Dy_2O@C_{80}$ found in DFT calculations (**conf 3** and **conf 4** have very similar arrangement of the Dy_2O cluster and are not distinguishable by eye). For the sake of comparison, orientation of the fullerene cage is the same in all figures. One of the symmetry planes of the cage is parallel to the paper, and the Dy_2O cluster in the lowest-energy conformer is lying in this plane.

CASSCF/SO-RASSI calculations of single-ion ligand field states

Single-ion magnetic properties were computed using MOLCAS at the CASSCF/SO-RASSI level with the (9,7) active space treating one Dy centre at a time and replacing the other Dy with Y, i.e. computations were performed for DyYO@C_{80} molecule, in which atomic coordinates were from the DFT-optimized Dy$_2$O@C_{80}.

Table S2. *Ab initio* computed ligand-field splitting energies for two Dy ions in Dy$_2$O@C_{2v}(5)-C$_{80}$, and their wavefunction composition in $|m_J\rangle$ basis

KD	E, cm^{-1}	Dy-1, $|m_J\rangle$ composition, %[a]	E, cm^{-1}	Dy-2, $|m_J\rangle$ composition, %[a]
1	0	99.8$|15/2\rangle$	0	99.9$|15/2\rangle$
2	409	97.6$|13/2\rangle$	419	99.3$|13/2\rangle$
3	779	90.6$|11/2\rangle$ + 6.0$|9/2\rangle$	798	96.5$|11/2\rangle$ + 2.4$|7/2\rangle$
4	1064	80.8$|9/2\rangle$ + 9.7$|7/2\rangle$ + 4.7$|11/2\rangle$	1088	53.4$|9/2\rangle$ + 37.1$|-9/2\rangle$
5	1243	68.6$|7/2\rangle$ + 13.7$|3/2\rangle$ + 6.9$|5/2\rangle$	1282	76.4$|7/2\rangle$ + 18.9$|3/2\rangle$ + 3.3$|11/2\rangle$
6	1325	35.9$|5/2\rangle$ + 33.0$|1/2\rangle$ + 18.5$|-5/2\rangle$	1372	48.8$|5/2\rangle$ + 34.8$|1/2\rangle$ + 7.3$|9/2\rangle$
7	1340	41.8$|3/2\rangle$ + 21.3$|1/2\rangle$ + 12.3$|-1/2\rangle$	1394	45.3$|1/2\rangle$ + 35.2$|-3/2\rangle$ + 10.4$|5/2\rangle$
8	1409	42.2$|3/2\rangle$ + 16.6$|1/2\rangle$ + 14.2$|-1/2\rangle$	1466	39.4$|3/2\rangle$ + 27.2$|-5/2\rangle$ + 16.2$|-1/2\rangle$
		d(Dy–O) = 2.0384 Å		d(Dy–O) = 2.052 Å
		KD-1		**KD-1**
g_x		0.000042171		0.000202639
g_y		0.000047903		0.000232279
g_z		19.867619380		19.869816558

[a] only 3 largest contributions are listed

Geometrical angle Dy–O–Dy: 145.2°
Angle between quantization axes of **KD-1** states: 143.1° (36.9°)

Magnetization relaxation times

SQUID magnetometry measurements were performed with Quantum Design VSM MPMS3 system. Magnetization decay curves such as shown in Fig. S6 were fitted with stretched exponential function:

$$M(t) = M_{eq} + (M_0 - M_{eq}) \exp\left[-\left(\frac{t}{\tau_M}\right)^{\beta}\right]$$

Where M_{eq} and M_0 are the equilibrium and initial magnetizations, respectively, τ_M is a characteristic relaxation time and β is an additional parameter that corresponds to the time-dependent decay rate. Determined relaxation times and β parameters are listed in Tables S3 and S4.
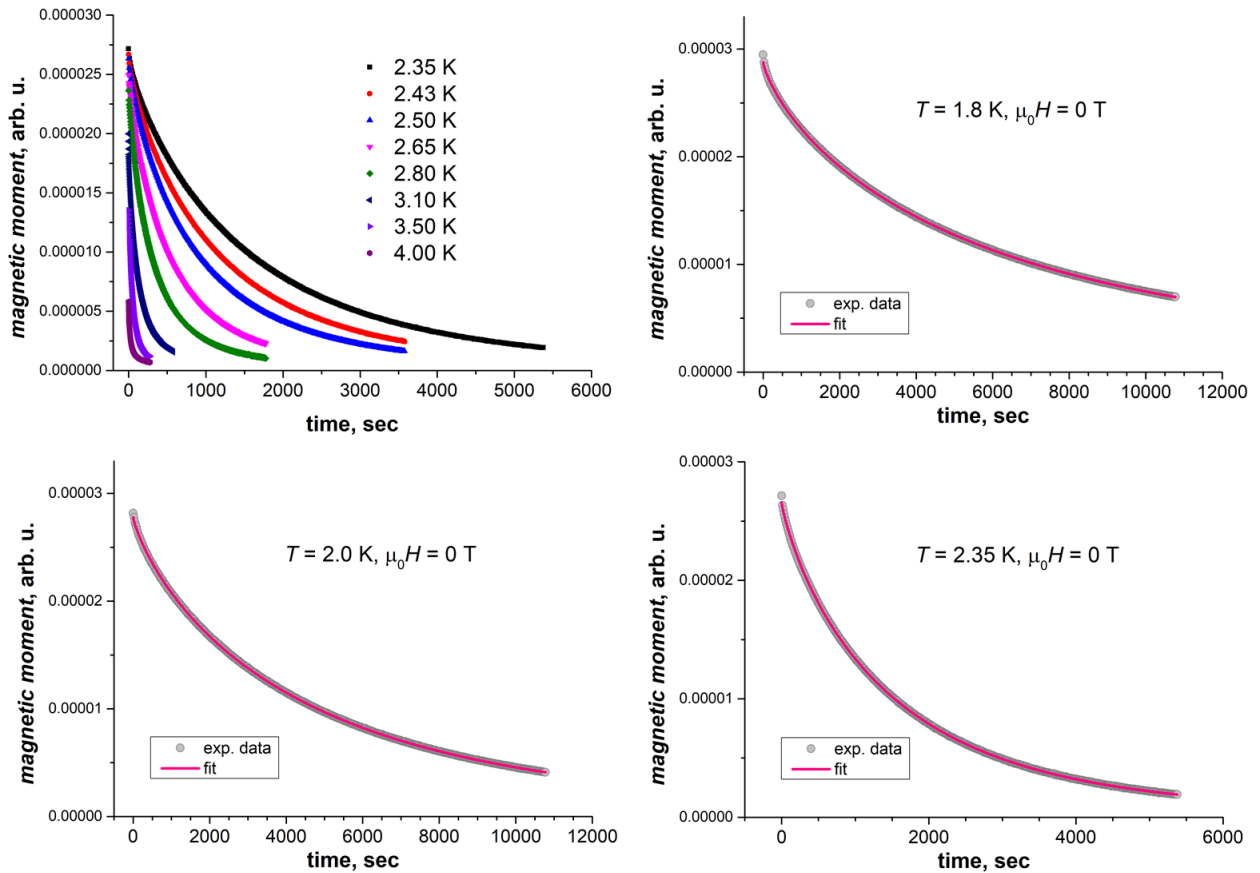
Figure S6. Representative magnetization decay curves measured in zero field at different temperatures and examples of fitting of experimental data with stretched exponentials.

Table S3. Magnetization relaxation times τ_M measured at different temperatures.*

T, K	τ_M, s @ 0 T	β	τ_M, s @ 0.1 T	β	τ_M, s @ 7 T → 2 T	β	τ_M, s @ 0 T → 2 T	β
1.8	5942	0.77	47863	0.52	45.5	1	185.3	0.53
1.85			26128	0.56				
1.9	5366	0.78	21445	0.60	47.0	0.65	218.5	0.51
1.95			13550	0.69				
2	4502	0.81	8366	0.75	45.8	0.77	172.6	0.60
2.1	3518	0.81	5833	0.81	48.1	0.66	202.7	0.56
2.2	2521	0.79	4124	0.80	46.6	0.57	175.1	0.65
2.27	2020	0.84	2938	0.81				
2.35	1522	0.84	2004	0.82	46.2	0.78	155.5	0.63
2.43	1143	0.84	1392	0.83				
2.5	888	0.82	1040	0.82	48.0	0.51	149.0	0.60
2.57	716	0.84	787	0.81				
2.65	524	0.84	567	0.83	42.0	0.75	110.9	0.71
2.7	432	0.87						
2.73	409	0.80	427	0.82				
2.8	320	0.77	331	0.80	45.0	0.74	105.0	0.76
2.9	248	0.82	239	0.84				
3	165	0.89	176	0.86	37.7	0.69	68.8	0.63
3.1	130	0.81	133	0.84				
3.25	97.9	0.83	88.7	0.85	33.1	0.55	74.6	0.65
3.37	70.5	0.82	70.3	0.82				
3.5	50.0	0.74	51.1	0.76	33.6	0.63		
3.65	44.1	0.78	39.6	0.86	37.0	0.59		
3.8	37.6	0.69	35.2	0.67	38.1	0.75		
4	23.2	0.56	25.2	0.57				

* 7 T → 2 T and 0 T → 2 T indicates measurements at 2 T after ramping the field from 7 T or from 0 T.

Table S4. Relaxation times τ_M measured at T = 2.5 K in different magnetic fields. Two sets are measurements for the field ramped from 7 T to the required values (7 T→μ_0H) and from zero field to the required value (0 T→μ_0H)

μ_0H, T	τ_M, s; 7 T→μ_0H	β	τ_M, s; 0 T→μ_0H	β
0.025	822	0.68	586	0.63
0.05	862	0.68	707	0.62
0.075	902	0.67	749	0.61
0.1	1050	0.84	1050	0.74
0.2	993	0.86	1011	0.75
0.3	892	0.85	858	0.68
0.4	743	0.83	737	0.75
0.5	625	0.82	638	0.73
0.6	525	0.78	525	0.76
0.7	439	0.76	412	0.68
0.8	382	0.72	366	0.74
1	284	0.66	273	0.69
1.2	252	0.65	218	0.68
1.4	217	0.70	183	0.65
1.6	143	0.58	166	0.64
1.8	72.8	0.67	155	0.62
2	44.9	0.58	149	0.60
2.2	49.5	0.56	148	0.59
2.3	92.5	0.69		
2.4	137	0.51	143	0.59
2.6	188	0.51	144	0.59
2.8	148	0.55	112	0.61
3	113	0.56	87	0.59
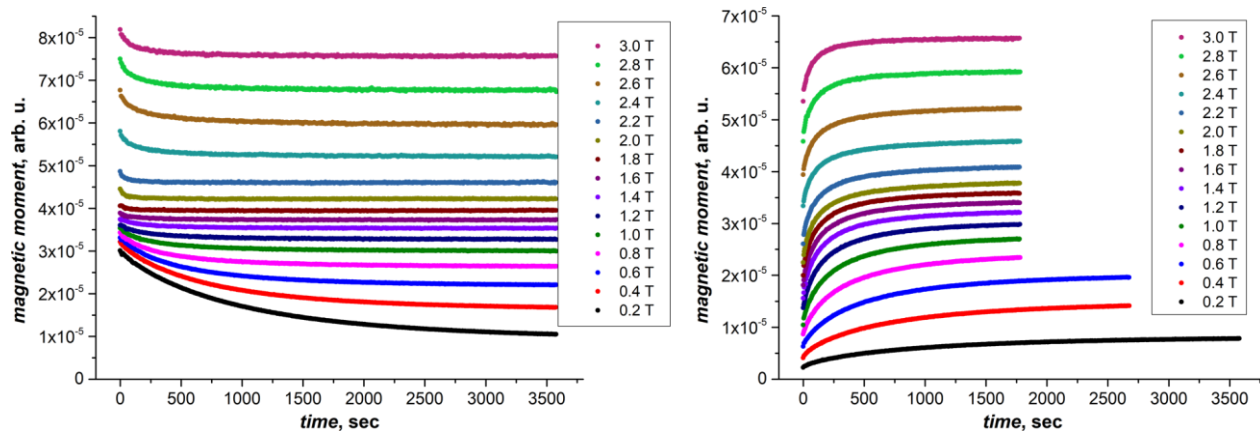
Figure S7a. Relaxation of magnetization at 2.5 K measured after ramping magnetic field from 7 T (left) and 0 T (right)
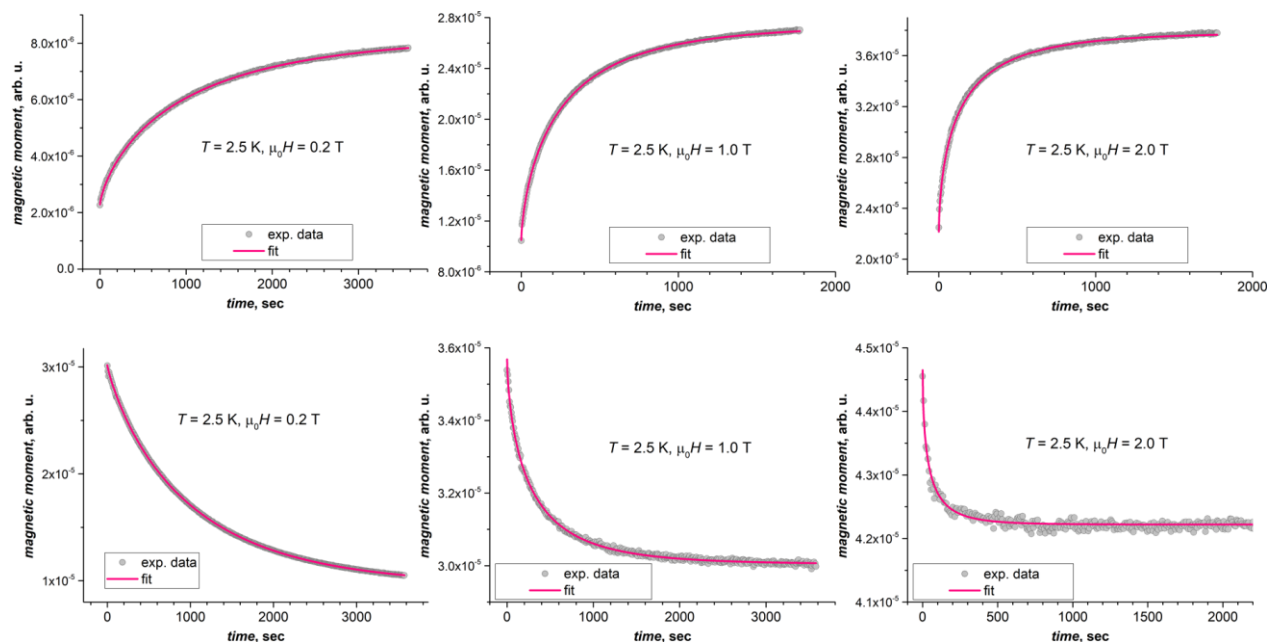
Figure S7b. Representative examples of fitting the curves from Fig. S7a with stretched exponential functions. Relaxation times and β parameters are listed in Table S4.

Additional discussion of relaxation mechanism

For the measurement of relaxation time at 2 T, we see almost no dependence for times measured after the field ramp from 7 T, but do observe some dependence for the measurements after the field ramp from 0 T. The temperature dependence can be described by a power function, $\tau_M^{-1} = CT^n$, with C = 0.0014±0.0003 s^{-1}K^{-n} and n = 1.91±0.24. The exponent is rather small, and can point to a direct mechanism or direct with phonon bottleneck, but the Raman contribution cannot be excluded ether. The difference of the temperature dependence of the relaxation time for the samples with different prehistory agrees with the absence of a sharp dip in relaxation times near 2 T for the times measured after the ramp from 0 T (and appearance of such a dip if the field is ramped from 7 T). Both phenomena indicate that after the ramp from 7 T, the main relaxation mechanism at 2 T is the QTM, whereas when the field is ramped from 0 T, the QTM is not that pronounced. However, we should note that in both cases the β values are rather small and the spread of values is also noticeable so that precise determination of the mechanism is hardly possible.

The different apparent mechanism for the decay and saturation of magnetization at 2 T may be preliminary explained as follows. When the field is ramped from 7 T, the system, which is in the |FM₊⟩ state, first goes through the |FM₊⟩↔|AFM₊⟩ crossing (point B in Fig. 5b), at which point partial equilibration should take place. But some molecules remain in the state |FM₊⟩ beyond this point and then undergo fast relaxation at the crossing of type |FM₊⟩↔|AFM₋⟩ (point A in Fig. 5b). This second process we observe with the dip of τ_M in the field dependence. When the field is ramped from 0 T, the first crossing type is |FM₊⟩↔|AFM₋⟩, but the equilibration to the state |AFM₊⟩ remains inaccessible for the QTM and requires thermal relaxation mechanism.

Magnetic measurements

The fullerene sample for magnetic measurements in the amount of ~0.1 mg was drop-casted onto quartz holder from CS_2 solution. The use of this sample preparation approach in the situation of the limited sample amount was found superior to the use of standard propylene capsules due to much lower background provided by homogeneous quartz holders. However, this technique limits the amount of the sample to ~0.1 mg because adhesion of the larger sample amount is not good enough and leads to detachment during the VSM measurement, whereas the use of glue or past again increases the diamagnetic signal. As this sample amount was not sufficient for reliable mass determination, in the fitting we relied on the shape of the magnetization curves rather than on the absolute signal.

Magnetic hysteresis and its derivative
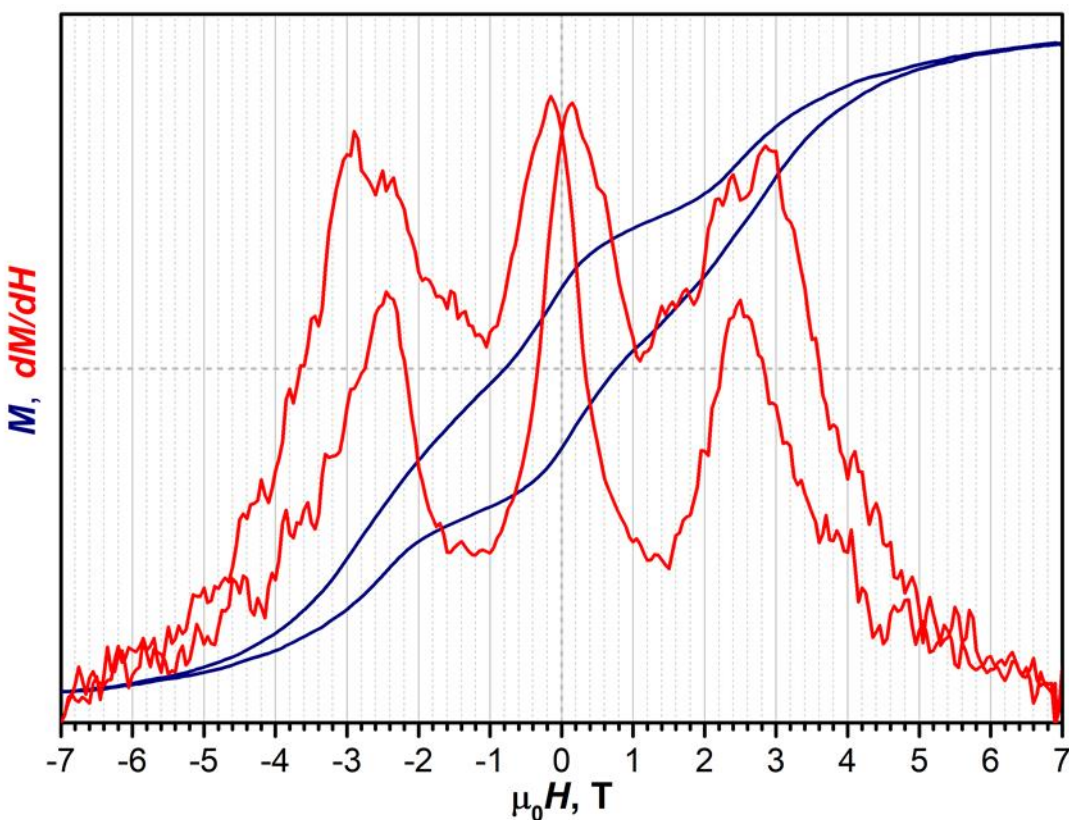
Figure S8. Magnetic hysteresis (dark blue) measured at 1.8 K and its derivative (red).

Fitting of magnetization curves
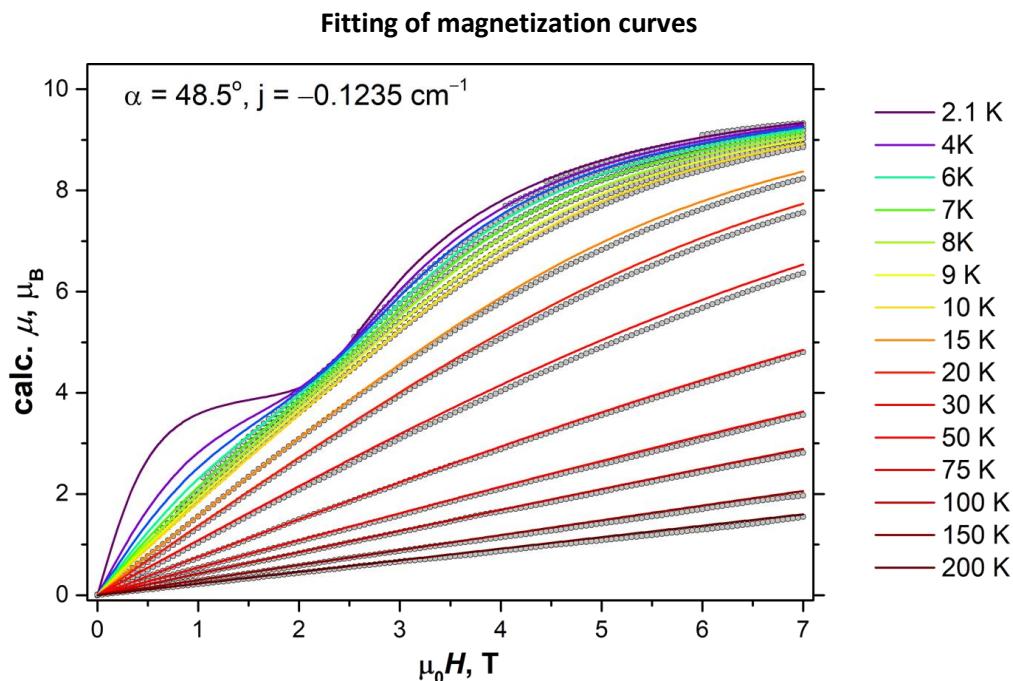
Figure S9. Experimental magnetization data used in the fitting (gray dots), and fitted calculated magnetization curves (colored lines) of $Dy_2O@C_{80}$. Note that the fit used only experimental data from the field range, at which magnetic hysteresis is already closed. This means that for the lowest temperatures only the highest fields (>5 T) were used.
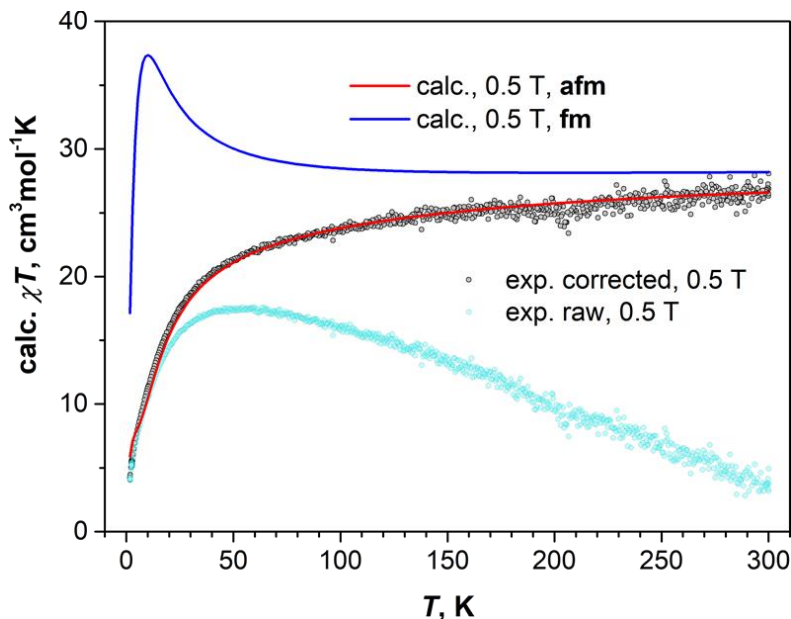
Figure S10. Comparison of experimental χT data to calculated ones. Magnetic susceptibility χ is defined as M/H, measured at 0.5 T, linear baseline correction was applied to correct for the diamagnetic drift (gray dots – after correction, light blue dots – raw data). Calculations were done for the fitted j_{12} and α parameters. In addition to $j_{12} = -0.12$ cm^{-1} (**afm** coupling), calculations were also performed for $j_{12} = +0.12$ cm^{-1} (**fm** coupling). The figure clearly shows that **fm** coupling should give a strong peak in the χT curve, which is not observed in experimental data.

Two types of Zeeman diagram and crossing histograms
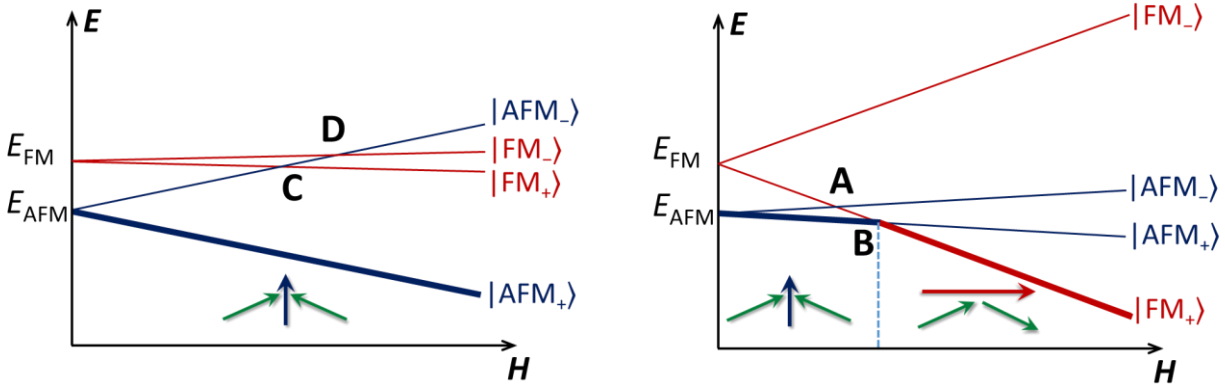
Figure S11. Zeeman diagram for $Dy_2O@C_{80}$ for two orientations of the magnetic field. Left: the field is nearly parallel to the magnetic moment of the AFM state; $|AFM_+\rangle$ remains ground state in all positive fields. Right: the field is nearly parallel to the magnetic moment of the FM state; $|AFM_+\rangle$ is the ground state in low fields, but $|FM_+\rangle$ becomes the ground state at higher fields, after level crossing of type B. In both figures, AFM and FM levels are plotted in red and dark blue, respectively. The ground state is highlighted by a thicker line.
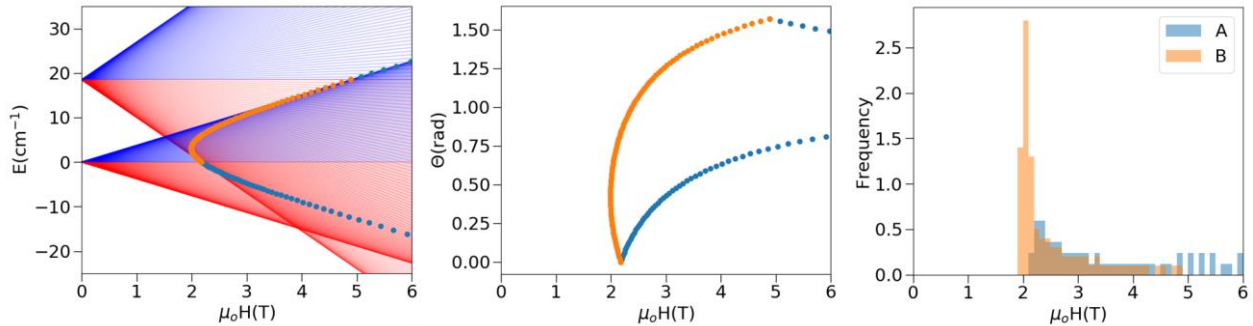
Figure S12. An overview of crossing events obtained with analytical model (i.e. considering that Dy moment are purely Ising spins). Note that crossing of type A (orange dots) has higher distribution density but is distributed in a narrower field range, whereas the crossing of type B (blue dots) has more sparse distributions but is distributed over a broader field range. This difference between A and B distributions depends on the angle between magnetic moments. The closer angle to 180°, the more different distributions are.